

# The Role of Lone-Pair Electrons in Pt–N Interactions for the Oxygen Reduction Reaction in Polymer Exchange Membrane Fuel Cells

Kahyun Ham,<sup>[a]</sup> Dongyoon Shin,<sup>[b]</sup> and Jaeyoung Lee<sup>\*[a, c]</sup>

An N-doped carbon with various N concentrations was prepared by using a scalable ball-milling method. The importance of the lone pair of electrons on the N species for the stability of Pt nanoparticles and their activity toward the oxygen reduction reaction was investigated. X-ray spectroscopic analysis

was used to investigate the interaction between Pt and the pyridinic N. The pyridinic N modified the Pt oxidation state and helped achieve size homogeneity and high catalytic activity by facilitating the rate-determining step.

## Introduction

Proton exchange membrane fuel cells (PEMFC) are a promising power source for transportation and stationary application with benefits such as high power density and low-temperature operation.<sup>[1]</sup> To date, platinum materials have demonstrated the highest catalytic activity toward oxygen reduction reaction (ORR) in fuel cells.<sup>[2–4]</sup> Because of the high price of Pt, a bottleneck in this area for commercialization is to lower Pt usage to  $<0.03 \text{ mg cm}^{-2}$  to curtail the production cost of the membrane electrode assembly (MEA). To reduce catalyst loading from current state of the art ( $0.05\text{--}0.1 \text{ mg cm}^{-2}$ ), the development of optimal catalysts using Pt<sup>[5]</sup> or non-PGM<sup>[6–10]</sup> such as Fe-N/C or heteroatom-doped carbon catalyst has continued on the basis of moderated oxygen binding strength on their surfaces to accelerate the sluggish kinetics of the oxygen reduction reaction (ORR) on the fuel cell cathode.

The doping of heteroatoms, especially nitrogen, into a carbon support has been shown to influence three aspects of the catalyst metal–support system: 1) the nucleation and growth rate during the synthesis step, 2) chemical binding between the metal catalyst and support, and 3) modification of the electronic structure of the metal. N species or defects pro-

duced during N insertion into a carbon lattice increase the interaction between the carbon support and Pt ions or Pt nanoparticles,<sup>[11]</sup> which is known to be responsible for improving durability and ORR activity.<sup>[12]</sup> However, the detailed roles of N species or defect to Pt in terms of oxygen binding energy have not been fully understood. It is also debatable whether the catalytically active site is only Pt or if it is accompanied with heteroatom-doped carbon, and this problem is challenging because of the homogeneity of N species prepared by different fabrication techniques.

Nitrogen doping can be performed through diverse in situ or ex situ processes. In situ doping requires the use of nitrogen precursor for the desired species and carbon prepared through the template method,<sup>[13,14]</sup> chemical vapor deposition,<sup>[15,16]</sup> and electrospinning,<sup>[17–21]</sup> whereas ex situ doping requires the incorporation of nitrogen dopant into an undoped carbon matrix such as through plasma coating<sup>[22]</sup> or thermal processing in ammonia or N<sub>2</sub>.<sup>[23]</sup> However, these methods need complex procedures and poisonous chemicals, which results in extremely low yields and limitation towards the commercial application of heteroatom-doped carbon materials. If the method includes pyrolysis, it is difficult to control the concentration of N species owing to evacuation of the N atom from the carbon lattice at high temperature. However, carbon materials for Pt nanoparticles support in fuel cells are necessary to increase the reaction surface area and decrease the Pt particle size. In addition to a high surface area, a support for fuel cells should also possess high electrical conductivity and a micro-/mesoporous structure to boost diffusion of the reactant species through the proton ionomers. Among various carbon materials, carbon black has been widely used owing to its high availability and low cost.<sup>[24]</sup> Baek and co-workers have proposed scalable production of edge-functionalized graphene through ball-milling.<sup>[25,26]</sup> The edge site in a carbon lattice can be substituted with H, S, N, I, Br, and other elements by cracking the graphitic C–C bond and inducing edge reactions through frictional heat with high energy. Along with nitrogen precursors such as pyridine and

[a] K. Ham, Prof. Dr. J. Lee

School of Earth Sciences and Environmental Engineering  
Gwangju Institute of Science and Technology (GIST)  
123 Cheomdangwagi-Ro, Gwangju 61005 (South Korea)  
E-mail: jaeyoung@gist.ac.kr

[b] Dr. D. Shin

Heterogeneous Reactions  
Max-Planck Institute für Chemische Energiekonversion  
34-36 Stiftstrasse, Mülheim an der Ruhr 45470 (Germany)

[c] Prof. Dr. J. Lee

Ertl Center for Electrochemistry and Catalysis  
Gwangju Institute of Science and Technology (GIST)  
123 Cheomdangwagi-Ro, Gwangju 61005 (South Korea)  
E-mail: jaeyoung@gist.ac.kr

Supporting Information and the ORCID identification number(s) for the author(s) of this article can be found under:  
<https://doi.org/10.1002/cssc.201903403>.

urea, large quantities of N-functionalized carbon material could be synthesized by mechanochemical ball milling. Recently, some research groups have succeeded in synthesizing N-doped carbon by using ball milling with melamine for use as a catalyst in an energy conversion system.<sup>[27–29]</sup> This scalable strategy is advantageous for the simple modification of pristine carbon black to edge-N-doped carbon as well as to achieve a high N doping concentration ( $\approx 10$  wt%); therefore, it is possible to use the N-doped carbon from ball milling as a catalyst support.

In this work, we investigated the ORR activity of Pt/N-doped carbon and its dependence on the N content. The activity of the ORR increased with the concentration of N species, especially pyridinic N. To investigate the role of the lone-pair electron in pyridinic N, we tuned the N content to determine the optimal Pt/N-doped carbon with high stability and activity in PEMFC.

## Results and Discussion

To investigate the structure of the N-doped carbon with respect to melamine content, we confirmed the chemical bond related with carbon by both X-ray photoelectron spectroscopy (XPS) in C 1s and X-ray absorption fine structure (XAFS) analysis in the C K-edge region. The XPS spectra in the C 1s region were obtained to examine the carbon species; five peaks at 284.6, 285.2, 286.4, 287.3, and 289.0 eV were assigned to carbon bonding as C=C  $sp^2$ , C=C  $sp^3$ , C–OH, C=O, and O–C=O, respectively [Figure 1(a)].<sup>[30]</sup> BMV (carbon without melamine) had a relatively high proportion of  $sp^3$  carbon, which might be owing to the defective structure compared with N-doped carbon, which predominant contained  $sp^2$  carbon. According to the Raman spectra of BMV (Figure S1 in the Supporting In-

formation), broader G and D bands were observed, which is generally observed in higher-disordered graphite with a high fraction of  $sp^3$  carbon.<sup>[31,32]</sup> 1.0MV and 3.0MV (N-doped carbon with a ratio of melamine to carbon black of 1.0 or 3.0, respectively) had a small amount of oxygen functional groups such as carbonyl groups (C=O), whereas BMV had a high concentration of C–OH and O–C=O groups in the carbon structure. The near-edge X-ray absorption fine structure (NEXAFS) spectrum of N-doped carbon with four peaks from A to D is shown in Figure 1(b).<sup>[33,34]</sup> The NEXAFS spectrum of BMV had a pre-edge at 283.7 eV (peak A), ascribed to missing carbon atoms and edge, as confirmed with the  $sp^3$  carbon peak in the C 1s XPS spectrum.<sup>[35]</sup> The pre-edge peak vanished in the spectra in the presence of melamine. Moreover, maximum intensities of 0.5MV, 1.0MV, and 3.0MV were observed at peak B for the  $\pi^*$  transition from C=C, whereas that of BMV shifted in the direction of high energy from peak B owing to the higher contribution of C–OH bonding (peak C).<sup>[36]</sup> Peak D at approximately 288.1 eV was assigned as unoccupied  $\pi^*$  from C–O–C and C–N bonding, and its intensities gradually increased with increasing melamine concentration.<sup>[37]</sup> To verify the origin of the C–O–C or C–N bond in NEXAFS spectra, we performed XPS analysis in the N 1s region, as shown in Figure 1(c), which was deconvoluted into four peaks: pyridinic N at 398.4 eV, pyrrolic N at 400.1 eV, graphitic N at 401.8 eV, and pyridinic N-oxide at approximately 405 eV. The nitrogen concentration increased from 2 to 11 at% with increasing melamine concentration, whereas the oxygen amount reduced accordingly, as determined by XPS (Table S1 in the Supporting Information). Therefore, peak D in the NEXAFS spectra could originate from C–N bonding of N-doped carbon synthesized in the presence of melamine, but it could be contributed by C–O–C in the case of BMV. The doping concentration determined by elemental analysis was approximately 11.59% in 3.0MV (Table S2 in the Supporting Information). The carbon edge of the oxygenated functional group (e.g., –OH and –C=O) of BMV could be induced by the carbon termination/oxidation reaction owing to the violent sparking by ambient air.<sup>[25,38]</sup> However, in the presence of melamine, the unstable carbon species could be modified to C–N bonding by triazine, which is generally used as an N-doping source and produced from melamine decomposition by frictional heat during ball milling. The pyridinic N and pyrrolic N were the main N species, which depended on the melamine concentration. The proportion of pyridinic N increased compared with that of pyrrolic N as the melamine concentration increased and was the highest in 3.0MV. After loading Pt nanoparticles on the as-prepared carbon support, XRD and TEM analysis was used to verify the Pt morphology and distribution.

The XRD patterns with respect to melamine concentration contained five distinct peaks at 39, 47, 67, 81, and 83° corresponding to Pt (111), (200), (220), (311), and (222), respectively [Figure 2(a)],<sup>[39,40]</sup> which was consistent with a face-centered crystal

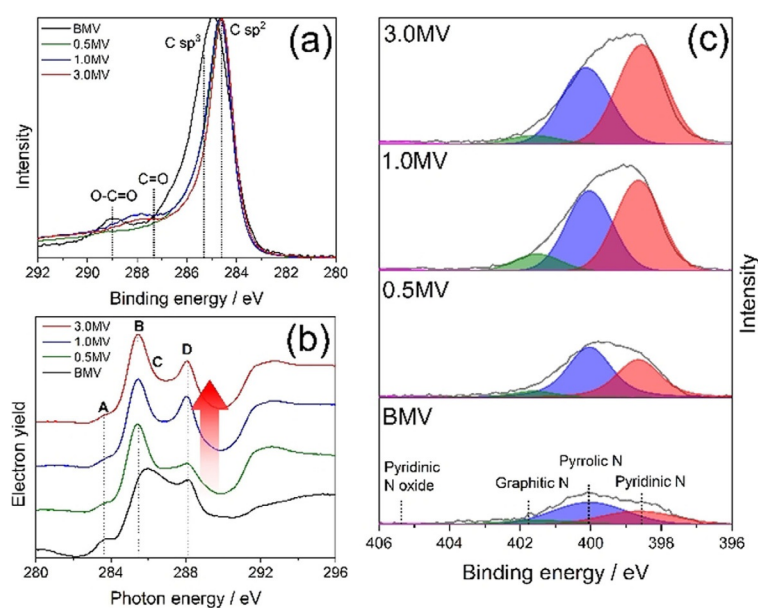


**Figure 1.** (a) C 1s XPS spectra, (b) NEXAFS spectra of the C K-edge, and (c) N 1s XPS spectra of N-doped carbon prepared with different amounts of melamine (BMV, 0.5MV, 1.0MV, and 3.0MV).

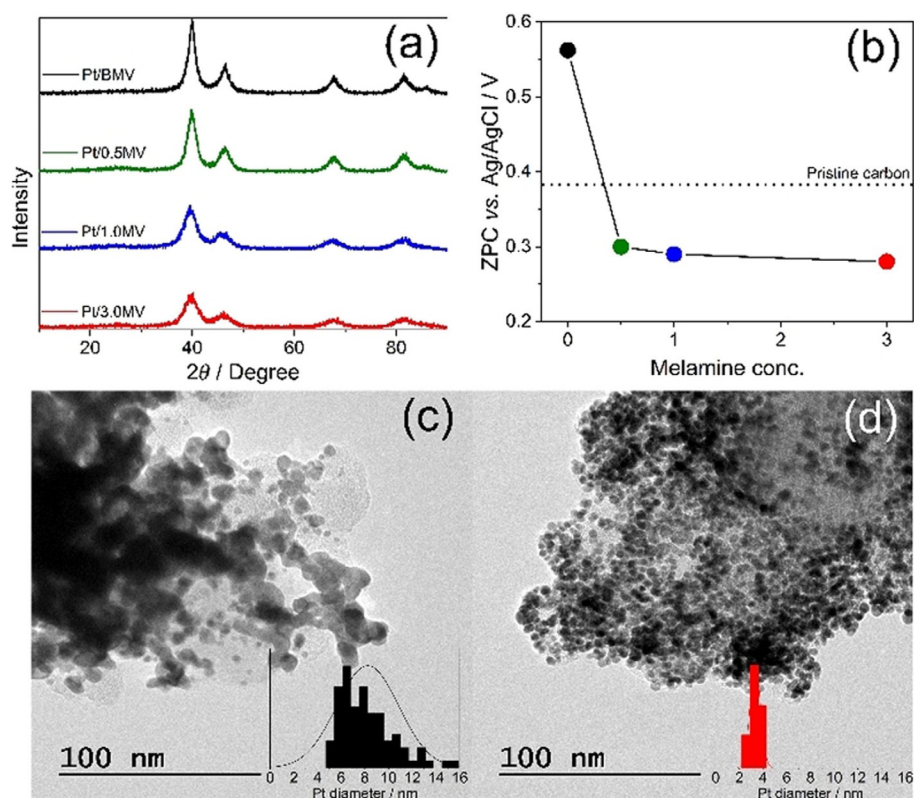


**Figure 2.** (a) XRD patterns of Pt/BMV, Pt/0.5MV, Pt/1.0MV, and Pt/3.0MV and (b) zero charge of potential (ZPC) depending on melamine amount (BMV, 0.5MV, 1.0MV, and 3.0MV). TEM images and (inset) histogram of Pt particle distribution of (c) Pt/BMV and (d) Pt/3.0MV.

structure of Pt. The full-width half maxima (FWHM) of the five peaks broadened with increasing melamine concentration, especially the (222) plane, which eventually disappeared in the XRD pattern of Pt/3.0MV. The (222) plane is parallel to the (111) plane, which is the predominant site in  $>2$  nm octahedral nanoparticles.<sup>[41]</sup> The average crystal size of the Pt nanoparticles was calculated with the (111) plane using Scherrer's equation and summarized in Table S3 in the Supporting Information. The domain size reduced from 5.52 nm in Pt/BMV to 2.91 nm in Pt/3.0MV. Support–metal interactions play an important role in determining the particle size and distribution because the support surface properties govern the nucleation and growth kinetics during metal deposition.<sup>[12]</sup> In terms of Pt amount, the amount of loaded Pt on N-doped carbon was almost similar to the melamine doping concentration, ( $50.5 \pm 0.6$ )% (Table S4 in the Supporting Information). The functional groups on the carbon support can affect Pt nucleation in terms of kinetics and strength between the Pt ion and carbon. To estimate the behavior of Pt and N-doped carbon during Pt nucleation, we compared the potential of zero charge (PZC), the potential region for minimum ion adsorption at the surface, depending on melamine concentration, as shown in Figure 2(b).<sup>[42]</sup> The PZC location was determined by the potential at minimum current, at which the adsorption of hydroxyl ion or chloride ion and oxidation of hydroquinone start, in cyclic voltammetry in  $N_2$ -saturated 0.1 M  $HClO_4$ . (Figure S2 in the Supporting Information).<sup>[43,44]</sup> In case of BMV, the PZC location positively shifted compared with the pristine carbon support. This

was interpreted as that the oxygenated functional groups withdraw anions on the surface of BMV owing to co-ion repulsion.<sup>[45,46]</sup> In contrast, N-doped carbons exhibited negative shift of the PZC location from the pristine carbon support, indicating the opposite surface charge against BMV was formed in 0.5MV, 1.0MV, and 3.0MV. According to the literature, oxygenated functional groups increase the acidity of the carbon surface, whereas N functional groups lead to the formation of basic groups, which increase the pH of the isoelectric point compared with pristine carbon.<sup>[47,48]</sup> In other words, the presence of nitrogen atoms from pyridine and pyrrole in 0.5MV, 1.0MV, and 3.0MV results in increased basicity of the N-doped carbon surface, and they act as nucleation sites, providing enhancement in the nucleation rate owing to their negatively charged and electron-rich donor surface state.<sup>[49,50]</sup> Therefore, if more N species are present in the carbon, the size of the Pt nanoparticles is smaller. The Pt nanoparticles in Pt/3.0MV were smaller (2.91 nm) than in Pt/1.0MV (2.98 nm) despite the similar N content. This could be related to the stability of the lone pair of electrons in pyridine and pyrrole. Pyridine has a stable conjugated system of three C=C bonds in the aromatic ring, and thus it has a free lone pair of electrons on the N atom for donation. In contrast, pyrrole does not have a conjugated system of  $\pi$  bonds owing to its pentagonal ring. Its lone pair of electrons participates in the resonance, so they cannot be donated with others. Pt/3.0MV had more pyridine, which could result in a more negatively charged surface, resulting in a smaller Pt nanoparticle size. As shown in Figure 2c,d and the inset image

of the Pt diameter histogram of Pt/BMV and Pt/3.0MV, Pt/3.0MV exhibited fine Pt nanoparticles with a uniform distribution, whereas the Pt nanoparticles agglomerated in the case of Pt/BMV. BMV also has a negatively charged surface incorporated in the oxygen functional group rather than the N species, but the higher electronegativity of the oxygen could excessively accelerate the nucleation kinetics and result in metal agglomeration.

We performed electrochemical tests to measure the electrochemical active surface area (ECSA) of Pt and evaluate the ORR activity depending on the N amount in carbon. A change in the peak shape of the cyclic voltammograms (CVs) owing to the presence of N species in the anodic current from 0.0 to 0.4 V vs. reversible hydrogen electrode (RHE) was observed [Figure 3 (a)]. The peak is known as hydrogen desorption from the Pt surface and used for measuring ECSA by calculating the peak area. The ECSA of Pt/3MV was higher than that of Pt/BMV owing to the small Pt size and uniform distribution confirmed by the TEM and XRD results. The ORR polarization curves are shown in Figure 3b, which indicated a lower onset potential as the amount of N species increased. In particular, Pt/3.0MV showed much higher ORR activity compared with commercial Pt/C. The uniformity of the Pt nanoparticles of Pt/3.0MV could contribute to this activity enhancement, but the

difference in ECSA was not sufficient to improve ORR activity. To determine the origin of the activity enhancement, we compared the activity of the carbon support because nitrogen functional groups are known as active material toward ORR owing to the presence of N–C sites.<sup>[51]</sup> However, as-prepared carbon supports were almost inactive in this acidic medium; consequently, the activity of Pt on N-doped carbon might be improved owing to other reasons rather than the synergetic effect between Pt and the nitrogen functional group.

Because the electronic configuration and electron density of d-orbitals is regarded as one of crucial parameters responsible for catalytic activity,<sup>[52]</sup> we investigated the Pt oxidation state and chemical bonding of the Pt atom. As shown in Figure 4(a), the peak positions of Pt on N-doped carbon were shifted to higher binding energy compared with Pt/BMV. This means that the Pt oxidation states were increased from Pt<sup>0</sup> to Pt<sup>2+</sup> or Pt<sup>4+</sup>. In contrast, the binding energies of nitrogen were negatively shifted (Figure S3 in the Supporting Information), which indicated that strong metal–support interaction happened, in agreement with the TEM image of well-distributed Pt particles on N-doped carbon. These metal f-band modification by N-doped carbon have been reported in several studies<sup>[53,54]</sup> and can result in changing of their catalytic activity by tuning the adsorption energy of the reactants and intermediates. Pyridine and pyrrole are known as electron donors. When Pt is deposit-

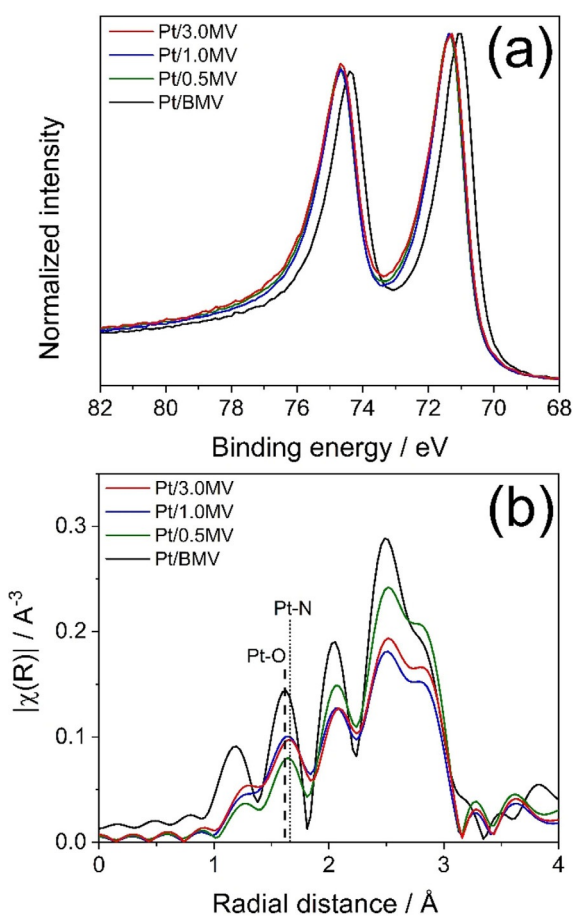


**Figure 3.** (a) XPS spectra of the Pt 4f region and (b) k<sub>3</sub>-weighted FT-EXAFS plots of Pt/BMV, Pt/0.5MV, Pt/1.0MV, and Pt/3.0MV.

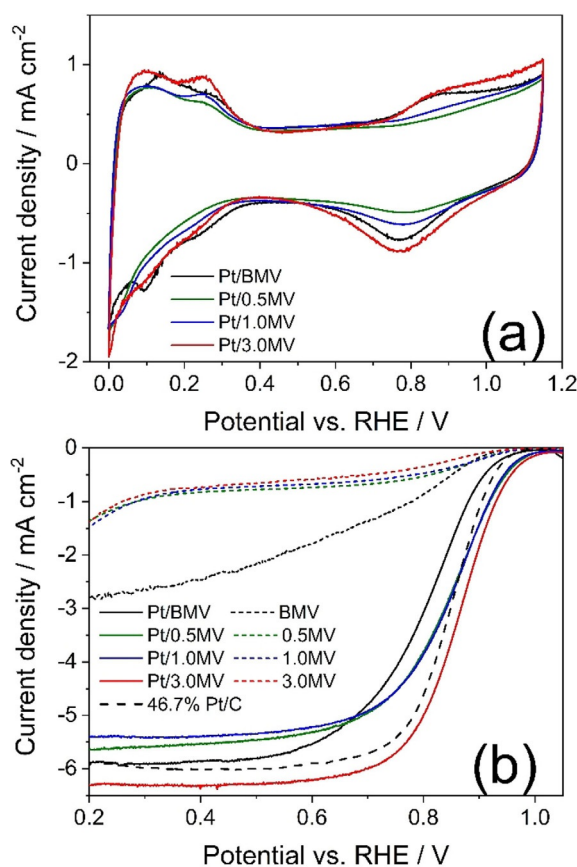


**Figure 4.** (a) CVs of Pt/BMV, Pt/0.5MV, Pt/1.0MV, and Pt/3.0MV in N<sub>2</sub>-saturated 0.1 M HClO<sub>4</sub> and (b) ORR polarization curves of Pt catalysts and their carbon supports in O<sub>2</sub>-saturated 0.1 M HClO<sub>4</sub> with 1600 rpm rotating speed.

ed, electron transfer from N species to unfilled orbitals of Pt could occur. However, the oxidation state of Pt was increased according to the XPS spectra. This discrepancy could be accounted by  $\sigma$ -bonding and  $\pi$ -backbonding from the lone pair of electrons in the  $\pi$ -orbital of the N atom in N species to the empty d-orbital of the Pt atom. Then,  $\pi$ -backbonding occurs from the filled Pt atomic d-orbital to the  $\pi$  antibonding orbital of the N atom.<sup>[55]</sup> Furthermore, we observed an increase in the radial distance of Pt–O in Fourier-transformed extended X-ray absorption fine structure (EXAFS) results obtained from the Pt–L edge (Figure 4b). The peaks at 2.64 and 1.64 Å were caused by Pt–Pt and Pt–O bonding, respectively.<sup>[56]</sup> As the N content in Pt on N-doped carbon increased, the intensity of the Pt–Pt bonding peak decreased, and the radial distance of the Pt–O bonding shifted to a more positive value. Because the atomic radius of nitrogen is bigger than that of oxygen, the increment might be owing to Pt–N bonding in Pt on N-doped carbon. We also performed electron paramagnetic resonance (EPR) analysis at room temperature to confirm Pt–N interaction (Figure S4 in the Supporting Information). The EPR signal was significantly reduced from 3.0MV to Pt/3.0MV. Because a large metal content is known to trigger fast relaxation of the conduction electrons,<sup>[57]</sup> the reduction in intensity was attributed to Pt loading on the C–N bond with an unpaired electron. Namely, most of the electrons in Pt/3.0MV existed in pairs and not unpaired electrons by formation of Pt–N interactions. In summary, the electrons of Pt on N-doped carbon might move from Pt to N owing to the formation of Pt–N bonding with strong electronic interaction. This tuned electronic structure through metal–support interaction might make a major contribution to enhancing the ORR activity by altering the activation energy of the ORR.

Two reaction steps are generally known to govern the ORR kinetics on Pt, which are the O–O bond cleavage step and the O<sub>2</sub> adsorption step accompanying charge transfer from the cluster to the adsorbate.<sup>[58]</sup> DFT calculations have revealed that Pt clusters on N species can make it easier for O<sub>2</sub> to adsorb and facilitate O–O dissociation by elongating the bond distance.<sup>[59]</sup> In the case of a Pt cluster on a pristine carbon support, the amount of transferred charge to O<sub>2</sub> is reduced because the Pt cluster also donates charge to the carbon support. That is, the presence of a carbon support diminishes the O<sub>2</sub> adsorption energy. It also leads to an increase in the Pt–O distance and a decrease in the O–O distance, and then causes sluggish ORR. In contrast, N species donate electrons to the Pt cluster. During ORR, electrons from the Pt cluster could transfer to O<sub>2</sub> and form a Pt–O bond. Therefore, enhanced ORR activity of Pt/3.0MV resulted from the electron donation from the N-rich carbon support to the Pt nanoparticles.

The decrease in the ECSA in the durability test of Pt/3.0MV, Pt/BMV, and commercial Pt/C is shown in Figure 5. It was assessed by using the triangle method, repeating CV from 0.6 to 1.0 V until 10000 cycles in O<sub>2</sub>-saturated 0.1 M HClO<sub>4</sub>. After 10000 cycles, Pt/3.0MV had an ECSA retention of approximately 90% of the initial ECSA, which was higher than that of commercial Pt/C. We also analyzed the concentration of dissolved Pt in 0.1 M HClO<sub>4</sub> after 10000 accelerated stress test (AST)

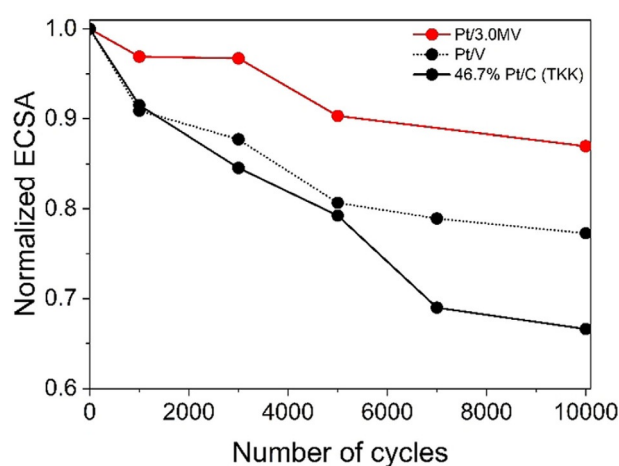


**Figure 5.** Normalized ECSA after a 10000 cycle durability test of Pt/BMV, Pt/3.0MV, and commercial Pt/C.

cycles using inductively coupled plasma (ICP)-MS. As summarized in Table S5 in the Supporting Information, dissolved Pt from Pt/3.0MV was much lower than from Pt/BMV. The Pt particle degrades mainly through dissolution from the Pt–OH form in this potential range of the durability test. The strong interaction between the Pt particle and N species in N-doped carbon might suppress Pt dissolution of Pt/3.0MV like in a previous study.<sup>[16]</sup> Pt/BMV, possessing oxygenated functional group, showed high Pt loss owing to promotion of the carbon corrosion process. It was reported that the incorporation of nitrogen into a carbon support leads to a reduction of oxygenated functional groups and inhibits Pt degradation against carbon corrosion.<sup>[60,61]</sup> We also performed TEM analysis to check the morphological change by an AST test. Even after 10000 cycles, Pt/3.0MV maintained its small particle size and uniform distribution owing to strong Pt–N interaction. (Figure S5 in the Supporting Information)

We evaluated the PEMFC performance and durability of Pt/3.0MV and Pt/BMV as cathode catalysts with 25 cm<sup>2</sup> of MEA. *I*–*V* curves were produced by using H<sub>2</sub>/air with various stoichiometry numbers in the cathode. 1.5 and 2.0 bar backpressure was applied to the anode and cathode, respectively. The open-circuit voltages, determined by mainly catalytic activity at low current density, of Pt/3.0MV and Pt/BMV were 0.923 and 0.878 V at the beginning of life, respectively (Figure S6 in the Supporting Information). This could contribute to enhanced ORR activity through a tuned Pt electron structure by N species in N-doped carbon. The performance in the high-current region of the *I*–*V* curve was affected by the MEA resistance and mass-transfer limitation. The steep slope in the *I*–*V* curve of Pt/BMV indicated a high contribution of the *iR* drop. When the quantity of oxygenated functional groups in a carbon support is increased, it has semiconductor-like electronic properties with a bandgap. However, nitrogen doping on carbon leads to narrowing of the bandgap or the formation of a new peak in the density of states around the Fermi level, which results in a system with metallic behavior.<sup>[58]</sup> Because of the high conductivity of 3.0MV, the rated power density was also higher

in Pt/3.0MV than in Pt/BMV. Furthermore, Pt/3.0MV retained a higher power density than Pt/BMV after 10 000 AST cycles owing to strong Pt–N interactions. As shown in Figure 6, the activity loss of Pt/3.0MV was only  $19 \text{ mW cm}^{-2}$ , whereas that of Pt/BMV was  $46 \text{ mW cm}^{-2}$ .

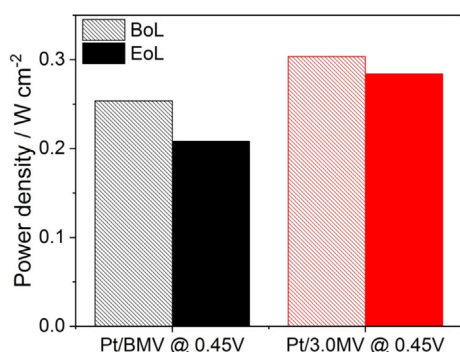


**Figure 6.** Power density at 0.45 V of a PEMFC cell voltage at beginning of life and after AST 10 000 cycles (end of life) of Pt/BMV and Pt/3.0MV.

## Conclusions

Pt nanoparticles were deposited on N-doped carbon fabricated through a facile and scalable ball-milling method. The amount of N increased with increasing amount of melamine precursor, especially the amount of pyridinic N. The lone pair of electrons of pyridinic N acted as the nucleation site for the Pt precursor, which led to a highly uniform distribution of fine Pt nanoparticles in the Pt/3.0MV catalyst. We confirmed the significance of the Pt–N bond in the Pt cluster depending on the N content by extended X-ray absorption fine structure (EXAFS) analysis and X-ray photoelectron spectroscopy (XPS). N species tether to the Pt nanoparticle by electron transfer through  $\pi$ -back-bonding. The tuned Pt electron structure contributes to enhanced oxygen reduction reaction (ORR) activity and proton exchange membrane fuel cells (PEMFC) performance. Furthermore, strong interaction between Pt and N-doped carbon prevents the loss of the Pt active surface area.

## Experimental Section

### Synthesis of N-doped carbon

The N-doped carbon was prepared through a ball-milling method with commercial carbon black (Vulcan XC-72, CABOT) and melamine (Sigma–Aldrich). Carbon black, melamine, and zirconia balls were mixed in a zirconia container. The weight ratio of carbon black to zirconia balls was 1:50. The concentration of N species in N-doped carbon was controlled by the ratio of melamine to carbon black as 0, 0.1, 0.5, 1.0, and 3.0. The mixture was pulverized in a planetary ball mill (Planetary Mono Mill, FRITSCH) with 500 rpm and 72 repetitions, including 30 min of milling and 10 min of pause time. To remove excess melamine in the produced carbon powder, it was washed in hot water and separated by vacuum filtration. Then, it was dried in an oven at  $60^\circ\text{C}$  for 24 h. The nitrogen content on the carbon was controlled by the ratio of melamine to carbon black. We designated the N-doped carbon de-

pending on the amount of melamine as BMV, 0.1MV, 0.5MV, 1.0MV, and 3.0MV.

### Synthesis of Pt/N-doped carbon

Pt nanoparticles on as-prepared N-doped carbon were synthesized through the polyol process. N-doped carbon (300 mg) was dispersed in a mixture of ethylene glycol (132.65 mL, Sigma–Aldrich) and deionized water (67.35 mL) using a bath sonicator for 1 h.  $\text{H}_2\text{PtCl}_6 \cdot x\text{H}_2\text{O}$  (Alfa Aesar) was dissolved in deionized water to make a 20% Pt precursor solution and diluted with ethylene glycol (20 mL, Sigma–Aldrich). The diluted Pt precursor solution was dropped into a carbon dispersion solution for 30 min, and then the solution was heated to reflux at  $160^\circ\text{C}$  for 3 h. When the temperature of the solution fell to  $40^\circ\text{C}$ , we increased the pH to 10 with 1 M NaOH solution (Sigma–Aldrich) and stirred the solution at  $40^\circ\text{C}$  for 20 h. Consequently, the Pt catalysts were obtained and labelled as BMV, Pt/0.1MV, Pt/0.5MV, Pt/1.0 MV, and Pt/3.0MV depending on the amount of melamine.

### Physicochemical characterization of N-doped carbon and Pt/C

We conducted various surface analyses of N-doped carbon, which can affect the Pt growth kinetics and chemical properties of loaded Pt on N-doped carbon. To determine the electronic structure and surface functional groups of N-doped carbon depending on the melamine content, NEXAFS spectra over the C K-edge were obtained at the total electron yield mode in beamline 10D located at Pohang Accelerator Laboratory (PAL). We also conducted XPS at Korea Basic Science Institute (KBSI) to investigate both N and C species and the elemental composition of N-doped carbon depending on the melamine content. In terms of the N amount, the weight percentages were also confirmed with an elemental analyzer (Elementar Analysensysteme GmbH). The carbon structure of N-doped carbon was observed with a Raman microscope (Horiba Jobin–Yvon). The excitation source was a 515 nm diode laser, and the excited laser was detected by a charge-coupled device (CCD) at room temperature.

The microstructure of Pt nanoparticles on N-doped carbon, such as the morphology and particle distribution, was analyzed by field-emission TEM (FE-TEM, JEM-2100F). The Pt loading amount was confirmed by ICP atomic emission spectrophotometry (ICP-AES, ACTIVA, JY HORIBA). The concentration of dissolved Pt ions in 0.1 M  $\text{HClO}_4$  after electrochemical AST test was analyzed by ICP-MS. Energy-dispersive X-ray spectroscopy was also utilized for the elemental atomic percentage and distribution. The crystal structure was confirmed by XRD (Miniflex II, Rigaku), using a  $\text{CuK}\alpha$  X-ray anodization source ( $\lambda = 0.15141 \text{ nm}$ ). The Pt oxidation state was determined by XPS at KBSI. XAFS in Pt L<sup>III</sup>-edge was also performed to investigate the chemical nature of Pt species of Pt nanoparticles on N-doped carbon. Spectra were obtained in TEY mode from beamline 7D of PAL. Powder-type specimens were collected in a sample holder to penetrate hard X-ray. EPR measurements were performed using a Bruker EMSPlex instrument. The microwave frequency was 9.644 GHz, and the power setting was 1 mW.

### Electrochemical measurements

Electrochemical tests were performed with a potentiostat/galvanostat (Biologic, VSP) and a three-electrode system consisting of Ag/AgCl (in 3 M KCl) and Pt wire as reference electrode and counter

electrode, respectively. A working electrode was fabricated by the ink drop-casting method. For the ink, catalyst (10 mg) was dispersed in a mixture of deionized water (1.2 mL), isopropanol (0.8 mL, Junsei), and Nafion resin dispersion solution (10  $\mu\text{L}$ , Sigma-Aldrich) in water and aliphatic alcohol. After dispersing for 30 min in a bath sonicator, catalyst ink (9.9  $\mu\text{L}$ ) was loaded on a rotating ring-disk electrode (RRDE, Pine, area = 0.248  $\text{cm}^2$ ) and then dried in an oven at 60  $^\circ\text{C}$  for 20 min. CV was performed in  $\text{N}_2$ -saturated 0.1 M  $\text{HClO}_4$  (Sigma-Aldrich) electrolyte from 0.05 to 1.15 V vs. RHE with a 20  $\text{mV s}^{-1}$  scan rate. The temperature of the electrolyte was maintained at 293 K with a circulator. For evaluating the ORR activity, linear sweep voltammograms (LSV) were acquired in  $\text{O}_2$ -saturated 0.1 M  $\text{HClO}_4$  electrolyte from 1.15 to 0.05 V vs. RHE with a 5  $\text{mV sec}^{-1}$  scan rate. Before CV and LSV, we conducted CV with a 100  $\text{mV sec}^{-1}$  scan rate in deaerated 0.1 M  $\text{HClO}_4$  electrolyte to remove organic chemicals from the ink solvent. The durability of Pt nanoparticles on N-doped carbon was assessed using a triangle wave cycle method, a kind of AST. This method involved repeated cycling from 0.6 to 1.0 V with a 50  $\text{mV sec}^{-1}$  scan rate, known as the Pt dissolution potential range. It was conducted in  $\text{O}_2$ -saturated 0.1 M  $\text{HClO}_4$  and included evaluation of the ECSA by CV and ORR activity by LSV every 1000, 3000, 5000, and 10000 cycles.

### PEMFC operation

To evaluate the performance in a PEMFC, we fabricated a MEA with 25  $\text{cm}^2$  of gas diffusion layer (29BC, SGL) and N211 membrane (Dufont). The catalyst was loaded by auto-spraying on gas diffusion layer (GDL) with catalyst ink, including catalyst, isopropanol, deionized water, and Nafion resin dispersion solution. Pt nanoparticles on N-doped carbon were used for only the cathode catalyst, whereas commercial Pt/C was used as the anode catalyst. The loading amount of the anode and cathode was 0.10 and 0.20  $\text{mg}_{\text{Pt}} \text{cm}^{-2}$ , respectively. Two GDLs with a catalyst layer were assembled with the membrane, then pressed with a hydraulic press system (3851-0, Carver) at 140  $^\circ\text{C}$ . The hot-pressing was continued for 5 min with 250 psi of pressure. The PEMFC test was performed with a fuel cell station (Scitech Korea Inc.). Prior to the  $I$ - $V$  curve measurement, we applied a constant voltage at 0.55 V for 4 h with blowing  $\text{H}_2$  and  $\text{O}_2$  gas to activate MEA by humidifying the membrane with water product. The cell temperature was maintained at 80  $^\circ\text{C}$ , and the relative humidity was 80%. We used  $\text{O}_2$  and air with a stoichiometry value of 2.0 to 4.0 as cathode fuel, whereas fixed  $\text{H}_2$  gas with 1.5 stoichiometry value was used in the anode for the  $I$ - $V$  curve measurements. In the case of PEMFC operation with air as cathode gas, backpressure was applied to make outlet gas pressure on the anode and cathode with 1.5 and 2.0 bar (abs), respectively. We increased 0.1  $\text{A cm}^{-2}$  every 20 sec from the open-circuit voltage to 0.3 V of the cell voltage. The AST test was performed by repeating a constant voltage at 0.6 V for 3 s and 1.0 V for 3 s as one cycle. The inlet gas was  $\text{N}_2$  gas for the cathode (50 sccm) and  $\text{H}_2$  gas for the anode (200 sccm). After 10000 cycle AST test, we obtained an  $I$ - $V$  curve to evaluate the performance at end of life.

### Acknowledgements

This research was supported by Technology Development Program to Solve Climate Changes through the National Research Foundation of Korea (NRF) funded by the Ministry of Science, ICT (2018- M1A2A2063861) and GIST Research Institute(GRI) grant funded by the GIST in 2020.

### Conflict of interest

The authors declare no conflict of interest.

**Keywords:** carbon materials · fuel cells · metal-support interaction · oxygen reduction reaction · platinum

- [1] A. Brouzgou, S. Q. Song, P. Tsiakaras, *Appl. Catal. B* **2012**, *127*, 371–388.
- [2] Y. Ha, S. Kang, K. Ham, J. Lee, H. Kim, *J. Phys. Chem. Lett.* **2019**, *10*, 3109–3114.
- [3] S. Chung, M. Choun, B. Jeong, J. K. Lee, J. Lee, *J. Energy Chem.* **2016**, *25*, 258–264.
- [4] S. Chung, D. Shin, M. Choun, J. Kim, S. Yang, M. Choi, J. W. Kim, J. Lee, *J. Power Sources* **2018**, *399*, 350–356.
- [5] J.-F. Huang, P.-K. Tseng, *Chem. Sci.* **2018**, *9*, 6134–6142.
- [6] D. Li, Y. Jia, G. Chang, J. Chen, H. Liu, J. Wang, Y. Hu, Y. Xia, D. Yang, X. Yao, *Chem* **2018**, *4*, 2345–2356.
- [7] N. Muthuswamy, M. E. M. Buan, J. C. Walmsley, M. Rønning, *Catal. Today* **2018**, *301*, 11–16.
- [8] H.-F. Wang, C. Tang, Q. Zhang, *Catal. Today* **2018**, *301*, 25–31.
- [9] N. Yang, L. Li, J. Li, W. Ding, Z. Wei, *Chem. Sci.* **2018**, *9*, 5795–5804.
- [10] Z. Xing, M. Xiao, Z. Guo, W. Yang, *Chem. Commun.* **2018**, *54*, 4017–4020.
- [11] D.-Y. Wu, B. Ren, Y.-X. Jiang, X. Xu, Z.-Q. Tian, *J. Phys. Chem. A* **2002**, *106*, 9042–9052.
- [12] Y. Zhou, K. Neyerlin, T. S. Olson, S. Pylypenko, J. Bult, H. N. Dinh, T. Gennett, Z. Shao, R. O'Hayre, *Energy Environ. Sci.* **2010**, *3*, 1437.
- [13] Y. Cheng, H. Lu, K. Zhang, F. Yang, W. Dai, C. Liu, H. Dong, X. Zhang, *Carbon* **2018**, *128*, 38–45.
- [14] J. Melke, B. Peter, A. Habereeder, J. Ziegler, C. Fasel, A. Nefedov, H. Sezen, C. Wöll, H. Ehrenberg, C. Roth, *ACS Appl. Mater. Interfaces* **2016**, *8*, 82–90.
- [15] D. C. Higgins, D. Meza, Z. Chen, *J. Phys. Chem. C* **2010**, *114*, 21982–21988.
- [16] Y. Chen, J. Wang, H. Liu, R. Li, X. Sun, S. Ye, S. Knights, *Electrochem. Commun.* **2009**, *11*, 2071–2076.
- [17] D. Shin, B. Jeong, B. S. Mun, H. Jeon, H.-J. Shin, J. Baik, J. Lee, *J. Phys. Chem. C* **2013**, *117*, 11619–11624.
- [18] B. Jeong, D. Shin, H. Jeon, J. D. Ocon, B. S. Mun, J. Baik, H.-J. Shin, J. Lee, *ChemSusChem* **2014**, *7*, 1289–1294.
- [19] B. Jeong, D. Shin, M. Choun, S. Maurya, J. Baik, B. S. Mun, S.-H. Moon, D. Su, J. Lee, *J. Phys. Chem. C* **2016**, *120*, 7705–7714.
- [20] D. Shin, X. An, M. Choun, J. Lee, *Catal. Today* **2016**, *260*, 82–88.
- [21] T. H. Vu, D. Shin, J. Jeong, J. Lee, *J. Phys. Chem. C* **2016**, *120*, 22342–22348.
- [22] S.-M. Kim, Y.-K. Heo, K.-T. Bae, Y.-T. Oh, M.-H. Lee, S.-Y. Lee, *Carbon* **2016**, *101*, 420–430.
- [23] S. Zhang, S. Chen, *J. Power Sources* **2013**, *240*, 60–65.
- [24] E. Antolini, *Appl. Catal. B* **2009**, *88*, 1–24.
- [25] I.-Y. Jeon, Y.-R. Shin, G.-J. Sohn, H.-J. Choi, S.-Y. Bae, J. Mahmood, S.-M. Jung, J.-M. Seo, M.-J. Kim, D. W. Chang, L. Dai, J. B. Baek, *Proc. Natl. Acad. Sci. USA* **2012**, *109*, 5588–5593.
- [26] I.-Y. Jeon, S.-Y. Bae, J.-M. Seo, J.-B. Baek, *Adv. Funct. Mater.* **2015**, *25*, 6961–6975.
- [27] R. G. Morais, N. Rey-Raap, J. L. Figueiredo, M. F. R. Pereira, *Beilstein J. Nanotechnol.* **2019**, *10*, 1089–1102.
- [28] Y. Xue, H. Chen, J. Qu, L. Dai, *2D Mater.* **2015**, *2*, 044001.
- [29] X. Fu, J. Jin, Y. Liu, Z. Wei, F. Pan, J. Zhang, *ACS Appl. Mater. Interfaces* **2014**, *6*, 3930–3936.
- [30] W.-S. Tseng, C.-Y. Tseng, C.-T. Kuo, *Nanoscale Res. Lett.* **2008**, *4*, 234–239.
- [31] K. N. Kudin, B. Ozbas, H. C. Schniepp, R. K. Prud'homme, I. A. Aksay, R. Car, *Nano Lett.* **2008**, *8*, 36–41.
- [32] A. C. Ferrari, J. Robertson, *Phys. Rev. B* **2000**, *61*, 14095.
- [33] K. Kaznatcheyev, A. Osanna, C. Jacobsen, O. Plashkevych, O. Vahtras, Ågren, V. Carravetta, A. P. Hitchcock, *J. Phys. Chem. A* **2002**, *106*, 3153–3168.
- [34] Y. Zubavichus, A. Shaporenko, M. Grunze, M. Zharnikov, *J. Phys. Chem. A* **2005**, *109*, 6998–7000.

- [35] W. Hua, B. Gao, S. Li, H. Ågren, Y. Luo, *Phys. Rev. B* **2010**, *82*, 155433.
- [36] H. B. Yang, J. Miao, S.-F. Hung, J. Chen, H. B. Tao, X. Wang, L. Zhang, R. Chen, J. Gao, H. M. Chen, L. Dai, B. Liu, *Sci. Adv.* **2016**, *2*, e1501122.
- [37] K. Kamiya, R. Kamai, K. Hashimoto, S. Nakanishi, *Nat. Commun.* **2014**, *5*, 5040.
- [38] I.-Y. Jeon, H.-J. Choi, M. Choi, J.-M. Seo, S.-M. Jung, M.-J. Kim, S. Zhang, L. Zhang, Z. Xia, L. Dai, N. Park, J.-B. Baek, *Sci. Rep.* **2013**, *3*, 1810.
- [39] M. A. Shah, *Sci. Iran.* **2012**, *19*, 964–966.
- [40] J. K. Lee, J. Lee, J. Han, T.-H. Lim, Y.-E. Sung, Y. Tak, *Electrochim. Acta* **2008**, *53*, 3474–3478.
- [41] M. Shao, A. Peles, K. Shoemaker, *Nano Lett.* **2011**, *11*, 3714–3719.
- [42] A. J. Bard, L. R. Faulkner, *Electrochemical Methods: Fundamentals and Applications*, Wiley, Hoboken, **2001**.
- [43] X. Gao, A. Omosebi, J. Landon, K. Liu, *J. Electrochem. Soc.* **2014**, *161*, E159–E166.
- [44] M. M. Lounasvuori, M. Rosillo-Lopez, C. G. Salzmänn, D. J. Caruana, K. B. Holt, *Faraday Discuss.* **2014**, *172*, 293–310.
- [45] E. Avraham, M. Noked, Y. Bouhadana, A. Soffer, D. Aurbach, *Electrochim. Acta* **2010**, *56*, 441–447.
- [46] I. Cohen, E. Avraham, Y. Bouhadana, A. Soffer, D. Aurbach, *Electrochim. Acta* **2013**, *106*, 91–100.
- [47] J. Amadou, K. Chizari, M. Houllé, I. Janowska, O. Ersen, D. Bégin, C. Pham-Huu, *Catal. Today* **2008**, *138*, 62–68.
- [48] L. Vaisman, G. Marom, H. D. Wagner, *Adv. Fun. Mater.* **2006**, *16*, 357–363.
- [49] Y. Zhou, R. Pasquarelli, T. Holme, J. Berry, D. Ginley, R. O'Hayre, *J. Mater. Chem.* **2009**, *19*, 7830.
- [50] J. D. Wiggins-Camacho, K. J. Stevenson, *J. Phys. Chem. C* **2009**, *113*, 19082–19090.
- [51] D. Guo, R. Shibuya, C. Akiba, S. Saji, T. Kondo, J. Nakamura, *Science* **2016**, *351*, 361–365.
- [52] *Theoretical surface science and catalysis—Calculations and concepts: B. Hammer, J. K. Nørskov in Advances in Catalysis, Vol. 45 of Impact Of Surface Science On Catalysis* (Eds.: B. C. Gates, H. Knozinger), Elsevier, San Diego, **2000**, pp. 71–129.
- [53] Y. Zhou, T. Holme, J. Berry, T. R. Ohno, D. Ginley, R. O'Hayre, *J. Phys. Chem. C* **2010**, *114*, 506–515.
- [54] Q. Shi, C. Zhu, M. H. Engelhard, D. Du, Y. Lin, *RSC Adv.* **2017**, *7*, 6303–6308.
- [55] R. Arrigo, M. E. Schuster, Z. Xie, Y. Yi, G. Wowsnick, L. L. Sun, K. E. Hermann, M. Friedrich, P. Kast, M. Hävecker, A. Knop-Gericke, R. Schlögl, *ACS Catal.* **2015**, *5*, 2740–2753.
- [56] N. Matsubayashi, H. Yasuda, M. Imamura, Y. Yoshimura, *Catal. Today* **1998**, *45*, 375–380.
- [57] L. Dennany, P. Sherrell, J. Chen, P. C. Innis, G. G. Wallace, A. I. Minett, *Phys. Chem. Chem. Phys.* **2010**, *12*, 4135.
- [58] T. Shinagawa, A. T. Garcia-Esparza, K. Takanabe, *Sci. Rep.* **2015**, *5*, 13801.
- [59] J. Ma, A. Habrioux, Y. Luo, G. Ramos-Sanchez, L. Calvillo, G. Granozzi, P. B. Balbuena, N. Alonso-Vante, *J. Mater. Chem. A* **2015**, *3*, 11891–11904.
- [60] M. Terrones, P. Redlich, N. Grobert, S. Trasobares, W.-K. Hsu, H. Terrones, Y.-Q. Zhu, J. P. Hare, C. L. Reeves, A. K. Cheetham, M. Ruhle, H. W. Kroto, D. R. M. Walton, *Adv. Mater.* **1999**, *11*, 655–658.
- [61] D. Mang, H. P. Boehm, K. Stanczyk, H. Marsh, *Carbon* **1992**, *30*, 391–398.

Manuscript received: December 12, 2019

Accepted manuscript online: January 10, 2020

Version of record online: February 19, 2020